

# Unveiling and Imaging Degenerate States in Plasmonic Nanoparticles with Nanometer Resolution

Viktor Myroshnychenko,<sup>\*,†</sup> Natsuki Nishio,<sup>‡</sup> F. Javier García de Abajo,<sup>§,||</sup> Jens Förstner,<sup>†</sup> and Naoki Yamamoto<sup>‡</sup>

<sup>†</sup>Institute of Electrical Engineering, Paderborn University, Warburger Straße 100, D-33098 Paderborn, Germany

<sup>‡</sup>Physics Department, Tokyo Institute of Technology, Meguro-ku, Tokyo, 152-8551 Japan

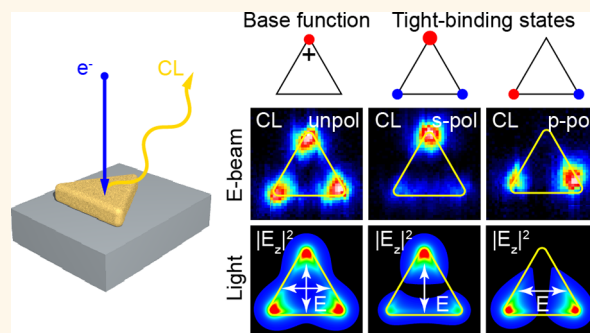
<sup>§</sup>ICFO-Institut de Ciències Fotoniques, The Barcelona Institute of Science and Technology, 08860 Castelldefels (Barcelona), Spain

<sup>||</sup>ICREA-Institució Catalana de Recerca i Estudis Avançats, Passeig Lluís Companys, 23, 08010 Barcelona, Spain

## Supporting Information

**ABSTRACT:** Metal nanoparticles host localized plasmon excitations that allow the manipulation of optical fields at the nanoscale. Despite the availability of several techniques for imaging plasmons, direct access into the symmetries of these excitations remains elusive, thus hindering progress in the development of applications. Here, we present a combination of angle-, polarization-, and space-resolved cathodoluminescence spectroscopy methods to selectively access the symmetry and degeneracy of plasmonic states in lithographically fabricated gold nanoprisms. We experimentally reveal and spatially map degenerate states of multipole plasmon modes with nanometer spatial resolution and further provide recipes for resolving optically dark and out-of-plane modes. Full-wave simulations in conjunction with a simple tight-binding model explain the complex plasmon structure in these particles and reveal intriguing mode-symmetry phenomena. Our approach introduces systematics for a comprehensive symmetry characterization of plasmonic states in high-symmetry nanostructures.

**KEYWORDS:** metallic nanoparticles, localized surface plasmons, cathodoluminescence, plasmon eigenmodes, symmetry, degeneracy, local density of optical states



Metal nanoparticles and fabricated nanostructures exhibit localized surface plasmon (SP) resonances<sup>1</sup> that render them valuable building elements for photonic devices and nanomaterials, allowing us to enhance, manipulate, and control light at the nanoscale.<sup>2,3</sup> These resonances oscillate at frequencies extending from the ultraviolet to the infrared domains and can be tuned over a broad spectral range by controlling the size, shape, composition, and dielectric environment of the structures.<sup>4–7</sup> Additionally, SPs can efficiently couple to external electromagnetic (EM) radiation and thus produce strong effects in the near- and far-field regions.<sup>8–10</sup> In particular, the overall functionality and optical response of nanoparticles strongly depend on structure symmetry, which enables the control of SP mode symmetry and frequency, as well as the spatial symmetry of the required excitation field.<sup>11–13</sup> This offers a practical way of focusing and enhancing EM energy around nanoparticles down to subdiffraction volumes in spatially selective and switchable ways as well as actively controlling the resulting angular radiation patterns.<sup>14</sup> These peculiar proper-

ties of nanoparticle plasmons find potential application in improved photovoltaics,<sup>15</sup> wave-guiding,<sup>16,17</sup> cancer therapy,<sup>18</sup> and optical sensing.<sup>19,20</sup>

A comprehensive insight into optical processes in plasmonic nanostructures and detailed knowledge of the EM field distribution associated with SPs confined spatially on length scales  $\sim 10$ s nm are of crucial importance for the development of these applications besides their interest from a fundamental viewpoint. The interaction of external EM radiation with metal nanoobjects can be probed in both the near-field and far-field domains. Substantial progress in understanding and controlling nanostructure optical properties has been driven extensively by the rapid development of several characterization techniques, such as optical spectroscopy,<sup>21–23</sup> near-field scanning optical microscopy,<sup>24,25</sup> two-photon luminescence microscopy,<sup>26,27</sup>

Received: May 24, 2018

Accepted: August 1, 2018

Published: August 1, 2018

photon-induced near-field electron microscopy,<sup>28,29</sup> and electron spectroscopy,<sup>30–32</sup> including electron energy-loss spectroscopy (EELS)<sup>33–38</sup> and cathodoluminescence (CL).<sup>39–45</sup>

However, despite the vast availability of these powerful experimental techniques, some fundamental properties of plasmonic excitations cannot be accessed directly or with a sufficient degree of spectral and spatial resolution. Although optical spectroscopy offers excellent spectral resolution, its spatial resolution in far-field optical imaging is constrained by the diffraction limit, and even near-field scanning optical microscopy with subdiffraction capabilities offers a spatial resolution on the order of 10s nm. In this respect, electron-based EELS and CL spectroscopies provide access to the spatial distribution of multipolar SP modes and optically dark modes<sup>46</sup> with sub-nanometer resolution.<sup>47–49</sup> However, the EELS and CL signals are insensitive to the phase of the field.<sup>50</sup> Moreover, while conventional EELS and CL give information related to the EM local density of optical states (LDOS), they are unable to separately image energetically degenerate SP resonances hosted in high-symmetry nanoparticles. We note that the electron beam couples to the EM field distribution of all possible plasmon modes sustained in a nanoparticle that are not excluded by symmetry at the specific beam position, and thus, the resulting plasmon map corresponds to the resulting mode superposition.<sup>36,51</sup> This may lead to an incorrect interpretation of the map and mode nature, finally resulting in a misleading understanding of the plasmon resonance behavior. Although selective excitation of degenerate modes has been recently demonstrated using a multilobed electron beam,<sup>50</sup> spatial imaging of degenerate modes remains a challenging task for electron-based methods. Furthermore, the energy resolution in EELS and CL is often too low to spectrally resolve and image closely spaced modes. Plasmon-band broadening in very dissipative metals can even mask and mix different modes, an effect that may hinder their identification and interpretation.

Here, we report on a comprehensive experimental and theoretical study of plasmonic-state symmetries in lithographically fabricated triangular gold nanoprisms by using CL spectroscopy performed on a STEM. This technique offers a rich source of information about the physics of SP modes, encoded in several optical degrees of freedom of emitted light, such as frequency, polarization, and linear momentum. Specifically, we use an 80 keV focused electron beam as a local broadband source of an evanescent EM field to excite multiple localized SPs over a broad spectral range. Induced optical radiation emitted from the sample is ultimately detected and imaged through angle- and polarization-resolved CL measurements. We demonstrate the great potential of this combined technique by revealing and accessing spatially resolved maps of multipolar SPs localized on individual nanoprisms with nanometer spatial resolution. We unveil the spatial distribution of degenerate SP states and show that the degeneracy can be classified and explored upon examination of the symmetry of their *s*- and *p*-polarized photon emission maps, which, in turn, grant us access into pure resonance eigenvectors and thus provide direct information about the EM LDOS. We analyze our results by comparing the experiment with full-wave electromagnetic simulations and a simple, although comprehensive, tight-binding model, which help us successfully explain the complex nature of the excited bright and dark plasmons in these nanoparticles and unveil

unexpected aspects of plasmon symmetry, including the appearance of the hexapolar mode at an energy lower than the quadrupolar mode. Finally, the combination of position-selective excitation with selective angular and polarization detection enables us to efficiently detect and image optically dark and out-of-plane modes, which are masked by more-dominant SP bands.

## RESULTS AND DISCUSSION

**Angle- and Polarization-Resolved Cathodoluminescence Spectroscopy.** We used a high-resolution electron-beam lift-off lithography to pattern gold equilateral triangular nanoprisms of 50 nm thickness and with varying edge lengths in the range of 100 to 400 nm on a 300 nm thick SiO<sub>2</sub> layer sputtered on a Si substrate. The localized SP resonances of such polycrystalline nanoparticles prevail in their optical response in the visible and near-infrared spectral ranges. To characterize the nanoprisms, CL experiments were performed using a JEM 2100F scanning transmission electron microscope (STEM) operated at 80 keV combined with a high-efficiency light detection system.<sup>52</sup> It is equipped with a field emission gun and a spherical aberration corrector that enable a probe size of 1 nm at the used accelerating voltage of 80 keV and beam current of the order of 1 nA. The light collimated by a parabolic mirror is directed outside the STEM through a lens, a polarizer, and a pinhole fixed on a XY stage to a spectrum analyzer with an electron-multiplying charge-coupled device (CCD) detector. This STEM-CL system can be operated in both monochromatic and panchromatic regimes and enables several measurement modes with space-, energy-, angle-, and polarization-resolved capabilities (see the [Methods](#) section).

The schematic of the experimental setup used and orientation of the sample with respect to the parabolic mirror is illustrated in [Figure 1](#). The *xyz* coordinates are fixed on the parabolic mirror, with the origin at the focal point of the

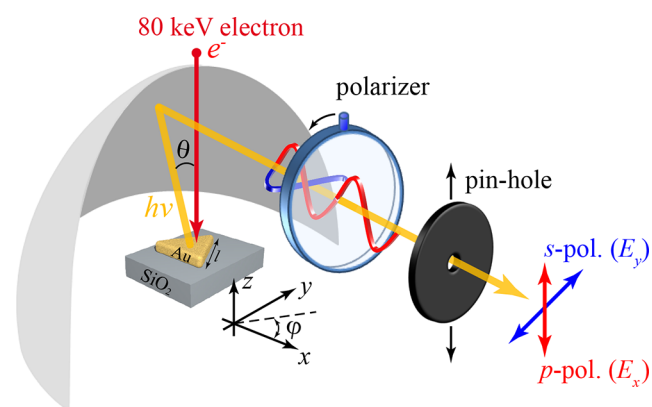


**Figure 1.** Schematic representation of our experimental setup. We measure angle- and polarization-resolved cathodoluminescence light emission assisted by excitation of localized plasmons by an 80 keV electron beam on an individual Au nanoprism lying on a SiO<sub>2</sub> substrate. A parabolic mirror collects and redirects the emitted light as a function of (i) emission direction (selected by a moving pinhole mask at angles  $\theta$  and  $\varphi$ ) and (ii) polarization (through a polarizer, which filters *p* and *s* light polarization components, parallel to the *xz* and *xy* planes, respectively). The electron beam (solid red arrow) impinges normally on the sample surface along the *z* axis and is raster-scanned along the *xy* plane. The nanoprism is oriented with one of its edges parallel to the axis of symmetry of the parabolic mirror (*x* direction).

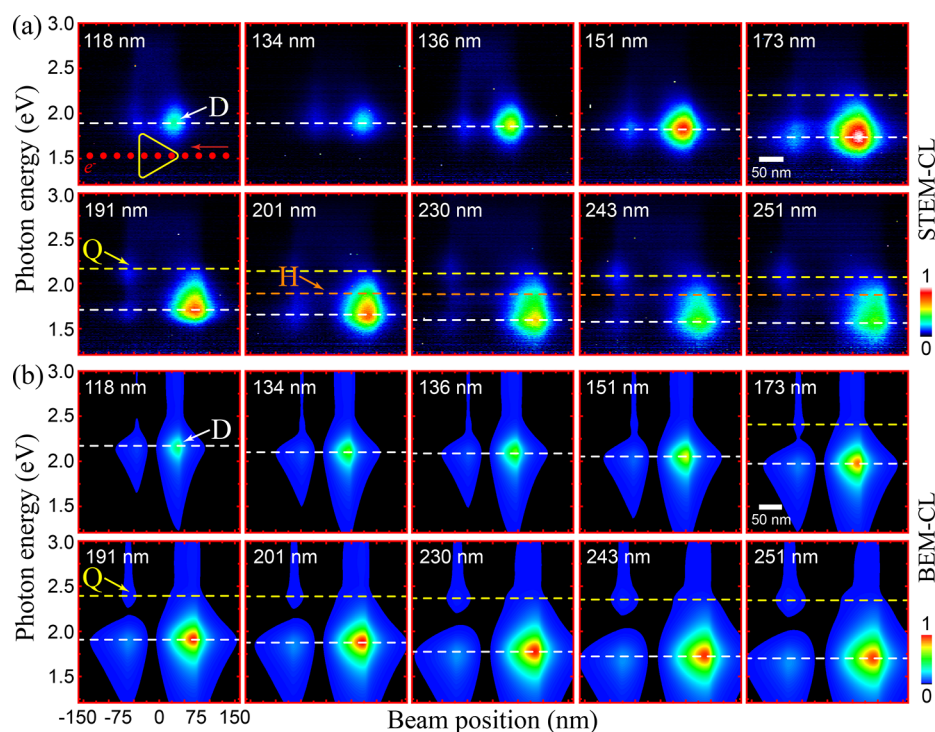


**Figure 2.** Plasmon dependence on nanoprism size. (a) Measured STEM-CL spectral images of unpolarized emission from individual gold nanoprisms with edge lengths in the 118–251 nm range. The images were recorded from nanoparticles oriented as shown in the inset to Figure 1 by scanning the electron beam along the red spots ( $y$  axis, horizontal direction in the plots) and taking a spectrum at each point (photon energy, vertical axes). The interaction of the nanoparticle with the electron beam leads to excitation of dipolar (D, white lines) and two higher-order (H and Q, orange and yellow lines, respectively) SP modes. (b) Calculations of the photon-emission probability corresponding to the spectral images in panel a, incorporating experimental setup parameters. Only the dipolar mode (D) and one nondipolar mode (Q) are resolved in the simulation. Experimental and theoretical images are normalized to a common color scale so that relative intensities are directly comparable.

parabola with the  $x$  axis oriented along the parabolic axis. A triangular nanoprism is oriented normal to the parabolic axis with one of its edges parallel to the  $x$  axis unless stated otherwise. The 80 keV electron beam is incident perpendicularly with respect to the nanoprism triangular base, i.e., parallel to the  $z$  axis. It excites the sample and the parabolic mirror collects and redirects the resulting radiation to the CCD detector through a moving pinhole mask and polarizer. In the present work, the pinhole with 2 mm diameter was set at the fixed position corresponding to the surface normal direction  $\theta = 0^\circ$ , which covers a solid angle of  $0.1\pi$  square radians unless otherwise stated. This ensures the symmetry of photon map patterns because all light emitted to any direction inside the solid angle can be detected. At each excitation position, an emission spectrum is recorded in the visible and near-infrared spectral ranges.  $P$ -polarized light has an electric field polarized parallel to the emission plane containing the surface normal direction and the emission direction, while  $s$ -polarized light is perpendicular to this plane as defined in Figure 1. The background radiation from the separately measured  $\text{SiO}_2/\text{Si}$  substrate is subtracted from the experimental data. To interpret experimental results and understand the nature of the electron-beam excited plasmon modes, numerical simulations of CL emission probability spectra and maps were performed using the retarded boundary element method (BEM).<sup>53–55</sup> The photon emission probability is given per incoming electron and per photon energy range. The emission is collected over the solid angle defined by polar angle  $\theta$  from  $0^\circ$  to  $18^\circ$  and azimuthal angle  $\varphi$  from  $0^\circ$  to  $360^\circ$  corresponding to the

experimental conditions unless otherwise stated (see the Methods section). The simulation is performed without account of substrate effects, which were studied in our previous work.<sup>36</sup> Experimental and numerical spectra are independently normalized to their own maximum peak intensities. Here, we focus on understanding the origin and symmetry of electron-driven individual-nanoprisms plasmons.

**Plasmon Modes in Individual Gold Nanoprisms.** We start our study of plasmonic modes in individual gold nanoprisms as a function of edge length  $l$ . Figure 2a shows the experimental beam scan spectral images obtained by scanning the electron beam along the bisector of each nanoprism (red spots in the inset) and simultaneously recording CL spectra for unpolarized emission at each point. These images allow us to detect regions on a nanoparticle in which different SP modes are preferentially and efficiently excited. Upon inspection, we observe that enhanced light emission occurs for electron-beam injection points in the vicinity of the corner at lower energies (white lines) and mid-edge at higher energies (yellow lines) but only for the larger nanoprisms (ca.  $l > 150$  nm). For now, we tentatively attribute the excitations at the lower and higher energies to the in-plane dipole (D) and higher-order (Q) SP modes, respectively. These experimental emission features are nicely reproduced by corresponding numerical simulations of the CL emission probability shown in Figure 2b. Additional weak emission at the energies in between those dominant modes is also observed in the experimental images (H, orange lines) when the beam is positioned near the center of much larger

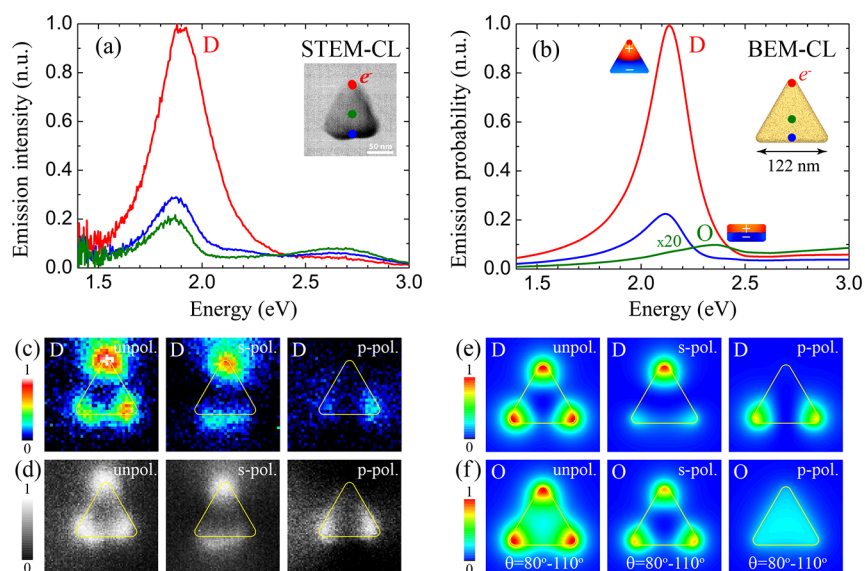


**Figure 3.** Spectral response and photon maps of a small gold nanoprism (side length  $l = 122$  nm). (a) Measured STEM-CL unpolarized photon-emission intensity spectra collected for different electron-beam probe positions, as shown on the BSE image inset. (b) Calculated emission spectra under the same conditions as in panel a. The in-plane (D) and weak out-of-plane (O) dipolar modes can be resolved in the simulation. The insets show the phase of the induced surface charge at the energies of the D and O modes. (c) Measured monochromatic photon maps of the D mode at the peak energy for un-, s-, and p-polarized emission. Each pixel is associated with a different position of the electron beam. (d) Corresponding experimental panchromatic (energy-integrated) photon maps. (e,f) Calculated photon emission probability maps of the modes (e) D and (f) O for un-, s-, and p-polarized emission as a function of electron probe position. (f) For mode O in panel f, the maps are constructed from the emission collected over a narrow range of polar angles  $\theta = 90^\circ \pm 10^\circ$ , where the mode reaches maximum radiation efficiency. The color scales in panels c–f are linear and common to all light polarizations.

nanoprisms (ca.  $l > 200$  nm). The evolution of the measured and calculated resonance energies and intensities of these modes is presented in Figure S1.

To analyze the features already suggested by Figure 2, in Figure 3, we present the study of emission from a small nanoprism with 122 nm edge length. Figure 3a shows the experimental unpolarized photon emission intensity spectra for electron beams focused at different positions, as indicated in a STEM backscattered electron (BSE) image of the sample in the inset. Only a dipolar mode D, involving collective conduction-electron oscillation in the plane of the triangle, is efficiently excited when the electron beam passes close to a corner of the nanoprism (red spectrum), in agreement with Figure 2. Our calculated CL photon-emission probability spectra taken at the same electron-beam positions (Figure 3b) are consistent with the experiment. They demonstrate mode D, whose frequency-resolved component of the phase of the charge density reproduces the dipole (see the inset). We attribute the red shift of the experimental peak D with respect to the calculated one mainly to the presence of the  $\text{SiO}_2$  supporting layer, which is not accounted for in the simulation. Additionally, imperfections in the geometry, uncertainties in morphological details, and surface roughness could also play a role. Figure 3c illustrates the experimental monochromatic photon maps of mode D for un-, s-, and p-polarized emission constructed by rastering the electron beam over the sampled area. These maps reveal the spatial dependence of mode D at its plasmon-resonance frequency, namely, the CL intensity reflects the electron-coupling efficiency, which is strong for electron positions where excitation of the mode is most efficient.<sup>40,56,57</sup> The CL map for unpolarized emission demonstrates highly localized photon emission maxima for electron-beam excitations at the prism corners, in agreement with previous works based on CL.<sup>36,42</sup> The strong photon

emission along the lower edge originates in the geometrical asymmetry of the nanoprism. Interestingly, the experimental panchromatic photon maps (Figure 3d), obtained by integrating the emission intensity over the wavelength and emission angle, almost identically replicate the corresponding monochromatic maps, confirming the dipolar plasmon-induced nature of luminescence in the small nanoprism. The calculated photon emission probability maps of mode D as a function of beam position over the sample (Figure 3e) are in good agreement with experimental counterparts for all emission polarizations. For now, we postpone our discussion of the maps for s- and p-polarized emission to later. Note that excitation at the nanoprism center leads to a weak out-of-plane dipolar mode O at  $\sim 2.37$  eV in the calculated spectrum only (Figure 3b, green curve).<sup>42,58</sup> Because the mode O is masked by the dominant band D, we constructed its spatially resolved photon maps by collecting the emission over a narrow range of polar angles,  $\theta = 90^\circ \pm 10^\circ$ , where the mode reaches maximum radiation efficiency (see Figure S2). The spatial variation of mode O is ultimately revealed in the map for its dominant p-polarized emission (Figure 3f), showing the expected constant intensity on the entire nanoprism. Surprisingly, the out-of-plane mode has not been detected in many previous works on noble-metal nanoprisms using EELS.<sup>33–36,38</sup>

We now extend our study to a large nanoprism with 266 nm edge length, as shown in Figure 4. Due to retardation effects in this case, the unpolarized emission spectra allow us to resolve, beside peak D, two additional resonance features H and Q in both the experiment (Figure 4a) and the simulation (Figure 4b). These multiple peaks are associated with in-plane EM eigenmodes of the nanoparticle because their energies decrease with increasing edge length. Measured and calculated spectra are in satisfactory agreement and show that the plasmon modes D, H, and Q are efficiently excited when the electron

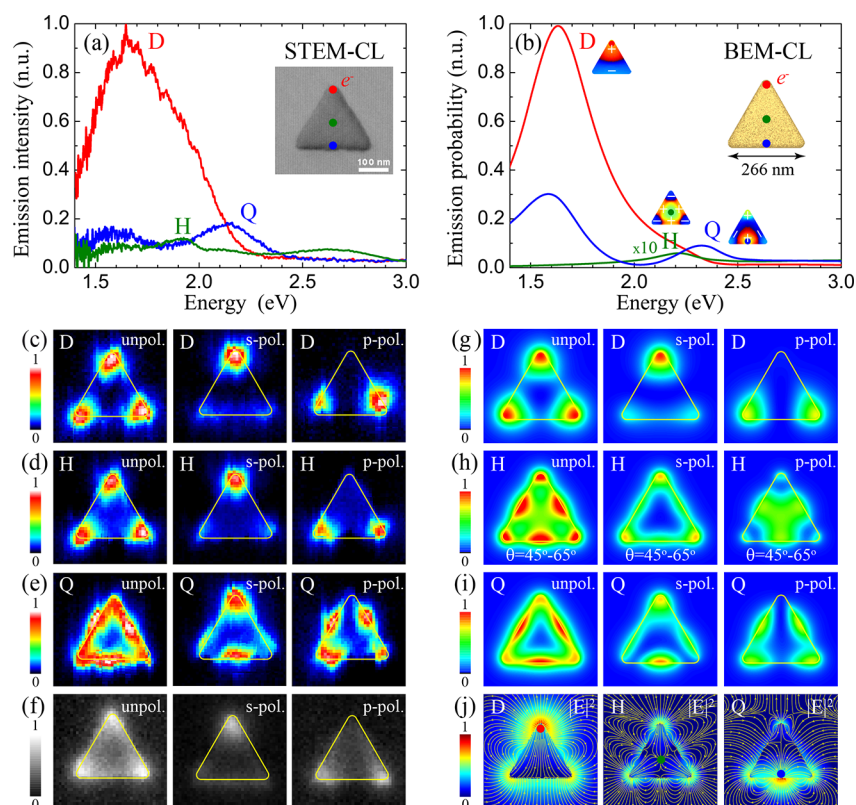


**Figure 4.** Spectral response and photon maps of a large gold nanoprism (side length  $l = 266$  nm). (a) Measured STEM-CL unpolarized photon-emission intensity spectra collected for different electron-beam probe positions, as shown on the BSE image inset. (b) Calculated emission spectra under the same conditions as in panel a. A total of three in-plane modes (D, H, and Q) can be resolved in both experiment and theory. The insets in panel b show the phase of the induced surface charge at the mode peak energy, as produced by the electron beam at the excitation positions indicated by colored dots. (c–e) Measured monochromatic photon maps of the modes (c) D, (d) H, and (e) Q at the peak energies for un-, s-, and p-polarized emission. Each pixel is associated with a different position of the electron beam. (f) Corresponding experimental panchromatic (energy-integrated) photon maps. (g–i) Calculated photon emission probability maps of the modes (g) D, (h) H, and (i) Q for un-, s-, and p-polarized emission as a function of electron probe position. Only for the maps of mode H in panel h, the emission is collected over the narrow range of polar angles  $\theta = 55^\circ \pm 10^\circ$  (disregarding mirror position), where the emission reaches its maximum. The color scale of the photon maps in panels c–i is linear and common to all emission polarizations. (j) Calculated electric near-field intensities  $|E|^2$  (log scale) and field lines of the components  $E_x, E_y$  in the  $xy$  plane at  $z = 0$  at the energies of modes D, H, and Q, as produced by the electron beam at the excitation positions shown by colored dots.

beam is focused at the corner (red spectrum), center (green spectrum), and mid-edge (blue spectrum) of the prism, respectively. The weaker mode H is masked owing to significant broadening of the dominant plasmon bands D and Q. Incidentally, the presence of the dielectric substrate in the experiment increases mode line widths as well as the prominence of higher-order modes (H and Q) and their mutual spectral separation in comparison to the simulation. The experimental monochromatic CL maps of these modes are shown in Figure 4c–e. Whereas mode D exhibits the enhanced emission at the corners, mode Q displays intensity enhancement at the corners and along edges of the particle. The spatial distributions of modes D and Q are resolved with nanometer resolution and are in excellent agreement with simulations for all emission polarizations (Figure 4g,i). Unlike the clearly distinct maps of modes D and Q, the experimental CL maps of the weaker mode H pick up some intensity from the dominant mode D as well. Therefore, like for mode O in Figure 3f, we construct maps of mode H in such a way that only the emission over a narrow range of polar angles  $\theta = 55^\circ \pm 10^\circ$ , where the mode reaches maximum radiation efficiency, is collected for each beam position (see Figure S3). This allows the reduction of the photon emission contribution from modes

D and Q. Indeed, the calculated spatial localizations of mode H for all light polarizations are well-resolved in Figure 4h (disregarding mirror position), exhibiting enhanced emission not only at the corners and along edges but also at the central area of the nanoprism. In particular, the CL map for p-polarized light emission nicely reproduces the corresponding experimental EELS map for noble metal nanoprisms.<sup>34,35,59</sup> Note that the emission features induced by all plasmons are clearly reflected in the experimental panchromatic images shown in Figure 4f, including a weak luminescence appearing at the nanoprism center due to mode H. To understand the origin of the detected modes, we calculated the phase maps at the peak energies induced by a passing electron at the corner, center, and mid-edge, where modes D, H, and Q are preferentially excited, respectively, as shown in the insets of Figure 4b. Notably, the “corner” mode D is clearly associated with charge pileup near the corners, whereas for the “edge” modes, namely H and Q, charges reside at the corners and mid-edges of the particle. Furthermore, Figure 4j shows the modes’ associated electric-field intensity maps  $|E|^2$  and field lines of the components  $E_x, E_y$  in the  $xy$  plane at  $z = 0$ . From the symmetry characteristics of the phase maps and field lines demonstrating 2-, 6-, and 4-fold symmetries, we can assign the

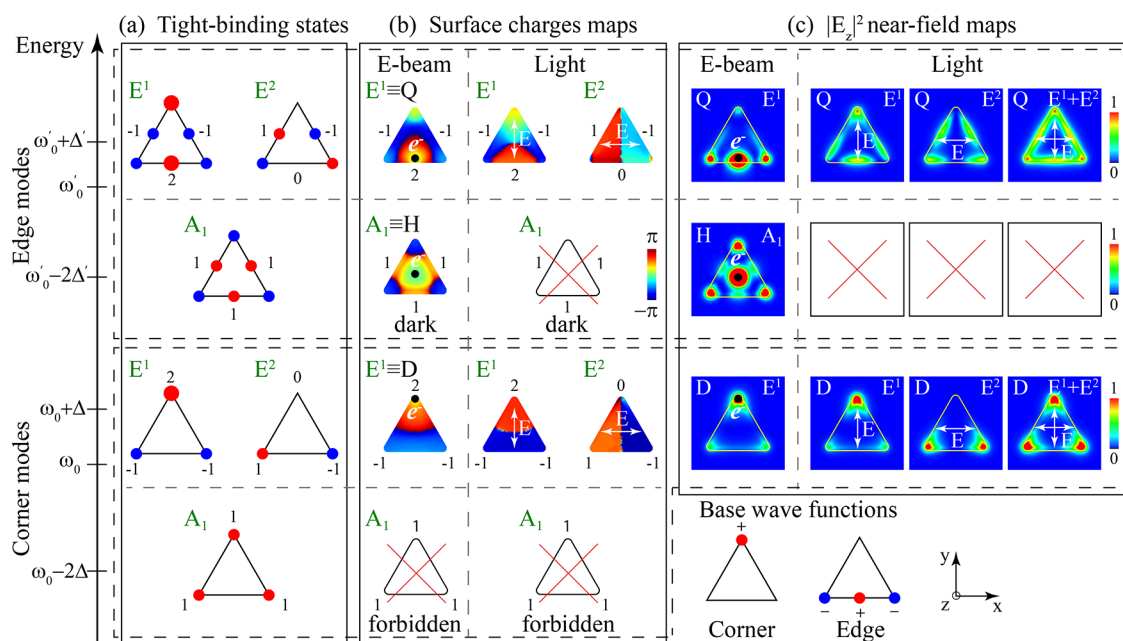


**Figure 5.** Symmetry, degeneracy, and energy of in-plane nanoprism plasmon modes explained with a tight-binding model. (a) Symmetry and energy of states in a triangular configuration obtained according to the tight-binding approach discussed in the main text, along with the corresponding Mulliken symbols (green labels). The basis functions used for corner and edges states are also shown at the bottom-right of this figure. (b) The contour plots on the left show the phase of the induced surface charge at the energy of corner (D) and edge (H and Q) modes corresponding to resonance features in the spectra of Figure 4b, as produced by the electron beam at the excitation position shown by a black dot in each plot. The symmetric corner mode is not physical because it involves a nonzero net charge on the particle, and so, it is absent in the spectra. Antisymmetric states (right column in panel a) of modes D and Q are not excited for the chosen electron-beam positions. The right panel shows phase maps of excited symmetric ( $E^1$ ) and antisymmetric ( $E^2$ ) degenerate states at the energy of modes D and Q, as calculated under optical excitation with the in-plane incident electric field polarized as indicated by the double white arrows. The symmetric edge mode (H) is optically dark and therefore absent from the optical spectra. (c) Calculated  $|E_z|^2$  near-field maps (linear color scale) of the modes in a  $xy$  plane situated 5 nm above the nanoprism, directly corresponding to the phase maps shown in panel b. The right column shows  $|E_z|^2$  intensity maps reconstructed by superposing the corresponding near-field maps of symmetric ( $E^1$ ) and antisymmetric ( $E^2$ ) modes, as produced by two plane waves with orthogonal polarizations. The prism edge length is 266 nm.

three detected peaks in the spectra to the in-plane dipolar (D), hexapolar (H), and quadrupolar (Q) modes, correspondingly. Counter-intuitively, the hexapolar mode H is spectrally located at the energy lower than the quadrupolar mode Q. In fact, in the majority of published articles on single triangular nanoprism spectroscopy, the first in-plane higher-order mode has been referred to as a quadrupolar mode, mainly in studies by far-field-based optical microscopies,<sup>4,21,22</sup> but it has been recast to a hexapolar mode in recent works using EELS.<sup>36,59,60</sup>

**Tight-Binding Model and Polarization-Resolved Maps of Eigenmodes.** To address these apparent and misleading discrepancies and explore the origin of  $s$ - and  $p$ -polarized CL maps, which have been missing from our discussion so far, we present an analysis based on a simplified tight-binding model in a nearest-neighbor approximation assuming that plasmons in a nanoprism are a linear combination of corner-bound states.<sup>55</sup> Using a quantum-mechanical notation, we consider one state,  $|n\rangle$ , localized at each of the corners,  $n = 1-3$ , with either positive or negative charge, assuming a common central frequency  $\omega_0$  for all of them plus some interaction  $V$  between nearest-neighbors corner states. We describe this interaction by a  $3 \times 3$  matrix of elements,  $\langle n|V|n'\rangle = 0$  for  $n = n'$  and  $\langle n|V|n'\rangle = -\Delta$  otherwise, where  $\Delta$  is a hopping frequency that represents the interstate coupling. Three eigenvalues and eigenvectors corresponding to the resonance energies of in-plane eigenmodes and the wave functions, respectively, are predicted upon diagonalization of this interaction matrix: one non-degenerate eigenmode,  $A_1$ ,

corresponding to perfectly symmetric combinations of the individual corner states oscillating at frequency  $\omega_0 - 2\Delta$  with equal weight in all corners,  $(1,1,1)$ , and a pair of doubly degenerate eigenmodes  $E^1$  and  $E^2$  at frequency  $\omega_0 + \Delta$  with weights  $(2,-1,-1)$  and  $(0,-1,1)$ , respectively. This is in full agreement with group theory description for our structure possessing a geometrical symmetry corresponding to the  $C_{3v}$  point group (considering the substrate), and therefore, we assign the eigenmodes in accordance with Mulliken's symbols.<sup>61,62</sup> The same analysis can be applied to explain edge modes, but now, the initial base functions are attached to two corners and the mid-edge position and, therefore, have zero net charge with a  $- + -$  profile along each individual edge. In this case, the linear combination of edge-bound states again leads to the non-degenerate eigenmode  $A_1$  and doubly degenerate eigenmodes  $E^1$  and  $E^2$  with the same eigenvectors as for the corner eigenmodes but with the higher central frequency  $\omega_0'$  and hopping  $\Delta'$ . Figure 5a schematically shows the states with weights obtained within the tight-binding approach for the corner (bottom part) and edge (upper part) base functions, which are also shown at the bottom-right of this figure.

The resulting eigenvector basis set at resonance energies can be well-represented by the induced surface charge of SP modes. Therefore, on the left panel of Figure 5b, we locate the electron-induced phase maps of the modes, demonstrated in Figure 4b, using the same labeling convention (D, H, and Q). The phase maps of modes D and Q clearly show the same

symmetry as the left-hand-side states ( $E^1$ ) of the corner and edge degenerate pairs, respectively, which are the only ones excited because the electron beam is placed at the axis of their mirror symmetry, i.e., at the upper corner and lower mid-edge, respectively. Evidently, the fully symmetric corner state  $A_1$  at frequency  $\omega_0 - 2\Delta$  has a nonzero net charge, so that it is unphysical and does not appear in the spectra. In contrast, the symmetric edge state  $A_1$  at frequency  $\omega_0' - 2\Delta'$  must be allowed now because the base functions have zero net charge along each edge, so the overall sum of the charges is zero. Indeed, the phase map of mode H, with opposite charges residing at the corners and mid-edges of the triangle, accurately reproduces the symmetry of this non-degenerate state. Thus, the order of the SP modes' spectral positions and their phase maps obtained from the simulations are in excellent correspondence with prediction from the simple tight-binding model, including the appearance of the hexapolar mode H at the lower energy than the quadrupolar mode Q. Interestingly, only the degenerate dipolar (D) and quadrupolar (Q) modes display finite net dipole moments and, consequently, couple strongly to far-field radiation, so they dominate the CL spectra in Figure 4. In contrast, the phase map of the non-degenerate hexapolar mode (H) has a vanishing in-plane dipole moment, and therefore, it is weakly coupled to radiation and appears only as a tiny feature in the spectra. Although optically dark, this mode can be excited by the electron beam and efficiently detected by collecting emission at larger polar angles  $\theta$  in the CL experiment. This explains why far-field-based optical microscopies miss the hexapolar mode. However, although EELS can access both bright and dark modes, because of the spectral proximity of quadrupolar and hexapolar modes, significant plasmon broadening and insufficient energy resolution, only the combined effect of both modes has been experimentally observed in gold and silver nanoprisms using EELS.<sup>36,38,59</sup> Indeed, the calculated EELS spectra shown in Figure S4 allow us to resolve distinct modes D, H, and Q, although modes H and Q strongly overlap. Furthermore, EELS maps of these modes are in good agreement with the corresponding CL maps for unpolarized emission (Figure 4g–i, left column). Interestingly, the out-of-plane mode O is also clearly detected in the EELS spectrum ( $\sim 2.4$  eV) for the excitation at the nanoprism center (green curve).

Note that the excitation of the mode with particular symmetry in a nanoparticle depends on the spatial symmetry of the excitation field as well.<sup>63</sup> In general, the incident electron beam focused at a particular position on a nanoparticle couples to all symmetry-allowed states at the particular position. Therefore, at the energy of the doubly degenerate mode (D or Q), it generally couples to both  $E^1$  and  $E^2$  states, and the excited surface charge distribution can be expressed as their linear combination. Otherwise, these degenerate states can be selectively excited by two properly chosen in-plane orthogonal linear polarizations of incident light.<sup>25,62</sup> In this case, the resulting phase maps of modes D and Q have the same symmetries as the degenerate tight-binding states. These are either symmetric ( $E^1$ ) or anti-symmetric ( $E^2$ ) with respect to the mirror symmetry plane, as depicted on the right panel of Figure 5b for comparison. For reasons that will become clear later, in Figure 5c, we also illustrate the calculated  $|E_z|^2$  near-field maps of the modes in a  $xy$  plane situated 5 nm above the nanoprism, which directly correspond to the phase maps shown in Figure 5b, i.e., the fields produced by the electron beam at the excitation position shown by a black dot in each

plot (left panel) and optical excitation with the in-plane incident electric field polarized, as indicated by the double white arrows (right panel). The right column shows  $|E_z|^2$  intensity maps reconstructed by superposing the corresponding near-field maps of  $E^1$  and  $E^2$  modes as produced by two plane waves with orthogonal polarizations.

We now turn to the interpretation of the polarization-resolved CL maps of SP modes shown in Figure 4g–i. The unpolarized CL maps of all modes in the nanoprism have the expected 3-fold symmetry, although in general, the orientation of the sample with respect to the mirror and range of collection angles used may result in asymmetry. Notably, the maps of the degenerate modes D and Q for  $s$ - and  $p$ -polarized emission possess only bilateral symmetry along the vertical axis of mirror symmetry, whereas the corresponding maps of the non-degenerate mode H exhibit 3-fold symmetry. Upon inspection, one notes that for both degenerate modes, the symmetries of their  $s$ - and  $p$ -polarized maps bear a striking resemblance to the tight-binding states  $E^1$  and  $E^2$ , respectively, and all maps of the non-degenerate mode display a resemblance to state  $A_1$  (see Figure 5a). Actually, it can be shown that for the 2-fold degenerate modes D and Q, the CL maps for  $s$ - and  $p$ -polarized emission reveal patterns representing the square of the absolute value of the eigenfunctions of pure states  $E^1$  and  $E^2$ , namely proportional to  $|\psi_{E^1}(\mathbf{R})|^2$  and  $|\psi_{E^2}(\mathbf{R})|^2$ , respectively, and their complete unpolarized CL maps can be represented by linear superposition of both corresponding eigenfunctions, i.e., by summing the corresponding CL maps for  $s$ - and  $p$ -polarized emission. In contrast, the unpolarized CL map of the non-degenerate mode H is governed by the eigenfunction of the single state  $A_1$ ,  $|\psi_{A_1}(\mathbf{R})|^2$ , where  $\mathbf{R}$  is the electron-beam transverse position; see the Supporting Information. Indeed, the CL maps of modes D and Q for  $s$ - and  $p$ -polarized emission faithfully reproduce the corresponding  $|E_z|^2$  near-field maps of eigenmodes  $E^1$  and  $E^2$  selectively excited by incident light, respectively, as shown at the right panel of Figure 5c (left and middle columns), and their CL maps for unpolarized emission (Figure 4g,i, left column) reproduce the corresponding superposed  $|E_z|^2$  near-field maps (Figure 5c, right column). In contrast, the CL map for the unpolarized emission of the non-degenerate mode H (Figure 4h, left column) closely replicates the corresponding  $|E_z|^2$  near-field map of eigenmode  $A_1$  obtained by electron-beam excitation at the nanoprism center (Figure 5c, left panel). Consequently, this proves that an unpolarized CL signal truly probes the  $z$  component of the radiative EM LDOS (along the electron path) because it is approximately proportional to the  $z$  component of the electric-field strength.<sup>64–66</sup>

#### Angle- and Polarization-Resolved Spectral Patterns.

So far, the small solid angle of emission collection in the backward direction was specially used to obtain spectra and symmetrical plasmon maps. However, as we already demonstrated, in this case, highly directional and weakly radiative modes might be missed or masked owing to plasmon broadening. Therefore, we additionally performed angle-resolved spectral (ARS) measurements, which provide a powerful instrument for detecting SPs in nanoparticles by analyzing far-field radiation patterns.<sup>67,68</sup> A nanoprism was rotated by  $90^\circ$  in an anti-clockwise direction around the  $z$ -axis from the configuration in Figure 1, i.e., the triangle faces the mirror. The spectra for a fixed electron-beam position were acquired by moving a 1 mm pinhole along the  $z$ -axis and

converting its position to the emission polar angles  $\theta = 0^\circ\text{--}90^\circ$  with the fixed azimuthal angle  $\varphi = 180^\circ$ . Figure 6a

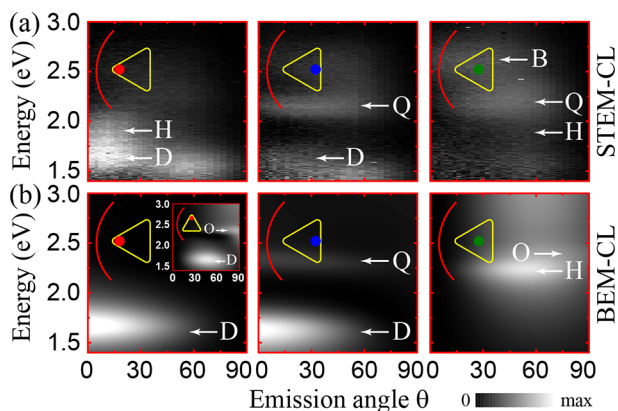


**Figure 6.** Angle- and polarization-resolved spectral measurements. (a) Measured angle-resolved spectral patterns (linear color scale) for a gold nanoprism of 255 nm side length and different electron-beam probe positions (see colored dots). The CL spectra for *p*-polarized emission are taken by scanning a 1 mm pinhole along the *z* axis, which is converted to emission polar angles in the  $\theta = 0^\circ\text{--}90^\circ$  range with fixed azimuthal angle  $\varphi = 180^\circ$  (see Figure 1). The 1 mm pinhole corresponds to a solid angle of 0.085 square radians at  $\theta = 0^\circ$  and 0.32 square radians at  $\theta = 90^\circ$ . The inset in each image shows the orientation of the nanoprism with respect to the mirror and the electron-beam position. Plasmon modes are indicated by labels assigned from their spectral locations in accordance with Figure 4. (b) Corresponding calculated patterns of the photon emission probability. The inset in the left image shows an angle-resolved spectral pattern for another nanoprism orientation but the same electron-beam probe position at the nanoprism corner (see inset).

demonstrates the experimental ARS patterns taken using the *p*-polarized emission for the electron beam fixed at the corner (left image), mid-edge (middle image) and center (right image) of the 255 nm nanoprism, as schematically depicted in the insets. Because the particle dimension is close to that in Figure 4, we expect the number of detected modes and their spectral positions to be preserved. Indeed, excitation at the prism corner gives rise to the dipolar mode (D), whereas excitation at the mid-edge leads to the clearly observed features of both dipolar (D) and quadrupolar (Q) modes, as named and denoted by arrows in the images. Unexpectedly, excitation at the nanoprism center results in the quadrupolar mode (Q), whereas the preferential hexapolar mode (H) is hardly detectable for this beam spot position, most likely due to the inaccurate positioning of the electron beam. Nevertheless, emission features of mode H appear as a shoulder to the dipolar mode in the pattern for the electron beam focused at the nanoprism corner, where electron coupling to the mode H is also efficient. Ultimately, additional feature B is also identified for the electron spot at the nanoprism center. It can be attributed to a higher energy radiative mode of thin films, like a Ferrell mode<sup>69</sup> or Brewster mode,<sup>70</sup> because it appears near the bulk plasmon energy ( $\sim 2.65$  eV) and its photon map has a constant emission profile over the entire nanoprism surface (see Figure S5). The bright contrast appearing around 1.5 eV could be due to the insufficient substrate subtraction. The calculated ARS patterns of the emission probability (Figure 6b) for excitations at the corner and mid-edge closely match those obtained from the

experiment. Moreover, precise positioning of the beam spot at the nanoprism center suppresses mode Q and enables us to resolve the hexapolar mode H and a rather weak profile of the out-of-plane mode O with their expected emission maxima at  $\theta \approx 55^\circ$  and  $\theta \approx 90^\circ$ , respectively. Thereby, all plasmon modes detected in Figure 4 are also resolved in ARS patterns in both experiment and theory, revealing their angular dependencies at respective plasmon-resonance frequencies. Finally, we note that the angular distribution of emission in an ARS pattern is strongly affected not only by the beam spot position but also by the nanoparticle orientation with respect to the mirror. This is illustrated in the inset of the left pattern in Figure 6b, showing the distinct emission distribution for another nanoprism orientation but the same beam position (see inset). In particular, the out-of-plane mode O, which is masked by the stronger quadrupolar mode Q in the spectra of Figure 4b, is now clearly detected.

## CONCLUSIONS

We have reported the application of angle-, polarization-, and space-resolved CL spectroscopy performed on a STEM to a comprehensive symmetry characterization of localized SP modes excited by electrons in gold nanoprisms. Our CL data have revealed that the nanoprisms accommodate bright dipolar and quadrupolar modes and, additionally, an optically dark hexapolar mode at energy lower than that of the quadrupolar mode. Interestingly, only one out of two higher-order modes supported by the particles has been detected and mapped in gold nanoprisms using EELS, which we attribute to insufficient energy resolution to resolve spectrally close modes. Remarkably, we directly access and image energetically degenerate dipolar and quadrupolar plasmonic eigenstates through our polarization-resolved measurements. The symmetry of CL maps for *s*- and *p*-polarized light emission measured with nanometer spatial resolution grants us access into pure resonance eigenvectors. Consequently, we have shown that CL maps for polarized emitted light directly reflect the corresponding spatial distribution of the projected radiative EM LDOS of each eigenmode.

Our understanding of the plasmon nature and symmetry has been also interpreted via a comprehensive tight-binding model that successfully explains the rich plasmon structure in these particles and reveals a complex interplay between symmetry-inactive, bright, and dark plasmon modes. This model is further supported by our simulations, which have allowed us to identify positions of electron-beam incidence, polarizations, and directions of light emission that permit efficiently detecting and imaging masked optically dark and out-of-plane weak-dipole modes by combining selective angle- and polarization-resolved measurements.

Although we only have considered triangular nanoprisms in this work, our approach to image degenerate and masked plasmons is general and can be applied to nanoparticles with other morphologies and symmetries. Essentially, the approach echoes selective excitation and near-field detection of plasmon modes using polarized light but with the ability to probe optical fields of plasmonic nanoparticles at the nanoscale. Overall, this work demonstrates that CL spectroscopy constitutes a powerful source of information that sheds light into the optical properties of highly symmetric structures. We anticipate that the method reported in this work will be useful in devising a suitable experimental setup for the selective retrieval of angular and polarization information on SPs.

## METHODS

**Sample Fabrication.** The gold triangular nanoprisms studied in this work were fabricated by electron-beam lift-off lithography using a positive resist layer (ZEP520A) and a 10 nm thick chromium sputtered layer as an adhesion layer on a 300 nm thick SiO<sub>2</sub> layer sputtered on a Si substrate. The nanoprisms had a height of 50 nm with various edge lengths in the range of 100 to 400 nm. They were aligned with an interval of 2 μm and fabricated under several electron-beam dosages from 120 to 200 μC/cm<sup>2</sup>. The prisms' corners were rounded with a curvature radius of about 10 nm. The edge lengths and corner curvature radii were measured from BSE images taken in the STEM.

**Cathodoluminescence Spectroscopy.** The experimental setup used to perform our CL experiments consists of a STEM (JEM 2100F) with an attached light detection system.<sup>49,52</sup> The STEM is equipped with a field emission gun (FEG) and a spherical aberration (Cs) corrector. In the system, a 9 mm gap pole-piece is used, and a parabolic mirror with a height of 8 mm is inserted in the gap. The focal length of the parabolic mirror is 3 mm. It is designed to locate the sample at the central position of the mirror, which enables light collection of both upper and lower spaces from the sample. The STEM can be operated at an accelerating voltage up to 200 keV, although in the present study, the CL experiment was performed at 80 keV to reduce sample damage due to electron irradiation. The usage of FEG and Cs corrector realizes a probe size of 1 nm, even at an accelerating voltage of 80 keV, and beam current of the order of 1 nA. The electron beam is focused onto the sample via a small hole in a parabolic mirror located directly above it. The mirror collects the light emitted from the sample and directs it out of the STEM through the lens, polarizer, and pinhole fixed on a X–Y stage. The pinhole can select light emitted from the sample with a special emission angle. The light passing through the pinhole is focused on a slit in front of a spectrometer by a second lens, and behind the spectrometer a spectrum is formed on a CCD element with 1024 channels in an EM-CCD detector (Andor DU970N). The utilized wavelength resolution of the light detector is 1 nm. However, if high resolution is needed, a 0.1 mm slit can be used for the spectrometer, which nominally gives a 0.4 nm resolution in wavelength. This CCD detector is mainly employed for photon mapping and angle-resolved measurements. Separate measurement of substrate light emission far from the nanoparticle enables background subtraction. The CL system enables the following three measurements with the angle-resolved capability. In beam scan spectral (BSS) measurement, CL spectra are recorded while scanning the electron beam along a certain line on the sample. The pinhole is fixed at a proper position (emission angle) during the measurement. A BSS image is a 2D pattern composed of the acquired spectra at the scanned beam positions. In photon-mapping measurements, the focused electron beam is scanned over certain area on the sample, while the emitted light passing through the monochromator allows CL spectra to be synchronously recorded at every pixel. The pinhole is fixed at a given position during the measurement. A monochromatic photon map at a certain energy is built up as a 2D image extracted from the acquired 3D data set. The acquisition time is 1 s per pixel in the present experiment. The photon mapping can be also performed in a panchromatic mode. In angle-resolved spectral (ARS) measurement, CL spectra are successively recorded while scanning the pinhole along a certain axis that corresponds to the change of the emission angle. The ARS pattern is a 2D data set consisting of spectra acquired at the pinhole positions corresponding to the emission angles. In this study, the pinhole moves in the vertical direction (*z* direction) that is normal to the sample surface, such that the direction of light emission detection is always parallel to the *xz* plane. Therefore, the *z* position of the pinhole corresponds to the polar emission angle  $\theta$ . The used diameter of the pinhole is 1 mm for the ARS measurements, corresponding to a solid angle of 0.085 square radians at  $\theta = 0^\circ$  and 0.32 square radians at  $\theta = 90^\circ$ . The intensity distribution in the experimental ARS patterns is corrected for this emission-angle dependence of the collection efficiency. The typical acquisition time for the ARS measurements is 3 s for each

spectrum. The beam position is fixed at a special position on the sample during the ARS measurements. The background intensity from the SiO<sub>2</sub>/Si substrate changes with the emission angle. Therefore, we first record an ARS pattern from the substrate and subtract it from the directly observed ARS pattern from the sample.

**Numerical Simulations.** Simulations of the EM response of self-standing gold nanoprisms are carried out using BEM.<sup>53–55</sup> This method is based upon rigorous solution of Maxwell's equations in frequency space, assuming that the materials involved in the structure are described in terms of local, frequency-dependent dielectric functions. The method allows us to exactly account for the size and shape of the nanoparticles by discretizing only boundaries separating different homogeneous media. The electron beam, moving with constant velocity  $\mathbf{v}$  in the *z* direction ( $\mathbf{v} = v\hat{z}$ ), is modeled using the electron charge density in frequency space  $\rho(\mathbf{r},\omega) = -(e/v)\delta(\mathbf{R} - \mathbf{R}_0)e^{i\omega(z-z_0)/v}$ , where  $\mathbf{r} = (\mathbf{R},z)$ ,  $\mathbf{R} = (x,y)$ ,  $\mathbf{R}_0 = (x_0,y_0)$  is the transverse location of the electron beam,  $e$  is the charge of the electron,  $\delta$  is the Dirac delta function, and  $v$  is the electron speed corresponding to an acceleration voltage of 80 keV. Once the solution of Maxwell's equations is found, the EM near- and far-fields induced by external fast electron excitation are calculated. The photon emission probability  $\Gamma_{\text{CL}}$ , which is proportional to the measured CL intensity, is calculated as  $\Gamma_{\text{CL}}(\Omega,\omega) = (1/(4\pi^2\hbar k))|f(\Omega)|^2$ , which represents the number of photons emitted per incoming electron and per unit of time, solid angle of emission,  $\Omega$ , and photon frequency range at frequency  $\omega$ . Here,  $k = \omega/c$  is the light wave vector,  $c$  is the speed of light in vacuum,  $\hbar$  is the reduced Planck constant, and  $f$  is the far-field amplitude. This equation is integrated over emission angles in accordance with the experimental setup to obtain CL intensities. The frequency-dependent dielectric function of gold is taken from measured optical data.<sup>71</sup>

## ASSOCIATED CONTENT

## Supporting Information

The Supporting Information is available free of charge on the ACS Publications website at DOI: 10.1021/acsnano.8b03926.

Details on the evolution of the measured and calculated resonance energies and intensities of SPs, detailed descriptions of the detecting and spatial imaging masked out-of-plane weak-dipole and optically dark hexapolar SPs, calculated electron energy-loss probability spectra and maps of the large gold prism, measured CL maps of the high-energy mode of the large gold nanoprism, and the relationship between eigenmodes in triangular prisms and a polarization-resolved CL signal. (PDF)

## AUTHOR INFORMATION

## Corresponding Author

\*E-mail: viktor.myroshnychenko@gmail.com.

## ORCID

Viktor Myroshnychenko: 0000-0001-6431-746X

## Notes

The authors declare no competing financial interest.

## ACKNOWLEDGMENTS

V.M. and J.F. acknowledge financial support from the Deutsche Forschungsgemeinschaft (DFG) via TRR142 project C05 and computing time at PC<sup>2</sup> Paderborn Center for Parallel Computing. F.J.G.deA. acknowledges funding from the Spanish MINECO (grant nos. MAT2017-88492-R and SEV2015-0522). N.N. and N.Y. acknowledge the Japanese MEXT Nanotechnology Platform (grant no. 12025014).

## REFERENCES

- (1) Bohren, C. F.; Huffman, D. R. *Absorption and Scattering of Light by Small Particles*; John Wiley and Sons, Inc.: New York, 1983.
- (2) Maier, S. A.; Brongersma, M. L.; Kik, P. G.; Meltzer, S.; Requicha, A. A. G.; Atwater, H. A. Plasmonics - A Route to Nanoscale Optical Devices. *Adv. Mater.* **2001**, *13*, 1501–1505.
- (3) Ozbay, E. Plasmonics: Merging Photonics and Electronics at Nanoscale Dimensions. *Science* **2006**, *311*, 189–193.
- (4) Kelly, K. L.; Coronado, E.; Zhao, L. L.; Schatz, G. C. The Optical Properties of Metal Nanoparticles: The Influence of Size, Shape, and Dielectric Environment. *J. Phys. Chem. B* **2003**, *107*, 668–677.
- (5) Burda, C.; Chen, X.; Narayanan, R.; El-Sayed, M. A. Chemistry and Properties of Nanocrystals of Different Shapes. *Chem. Rev.* **2005**, *105*, 1025–1102.
- (6) Liz-Marzán, L. M. Tailoring Surface Plasmon through the Morphology and Assembly of Metal Nanoparticles. *Langmuir* **2006**, *22*, 32–41.
- (7) Noguez, C. Surface Plasmons on Metal Nanoparticles: The Influence of Shape and Physical Environment. *J. Phys. Chem. C* **2007**, *111*, 3806–3819.
- (8) Myroshnychenko, V.; Rodríguez-Fernández, J.; Pastoriza-Santos, I.; Funston, A. M.; Novo, C.; Mulvaney, P.; Liz-Marzán, L. M.; García de Abajo, F. J. Modelling the Optical Response of Gold Nanoparticles. *Chem. Soc. Rev.* **2008**, *37*, 1792–1805.
- (9) Schuller, J. A.; Barnard, E. S.; Cai, W.; Jun, Y. C.; White, J. S.; Brongersma, M. L. Plasmonics for Extreme Light Concentration and Manipulation. *Nat. Mater.* **2010**, *9*, 193–204.
- (10) Halas, N. J.; Lal, S.; Chang, W. S.; Link, S.; Nordlander, P. Plasmons in Strongly Coupled Metallic Nanostructures. *Chem. Rev.* **2011**, *111*, 3913–3961.
- (11) Brandl, D. W.; Mirin, N. A.; Nordlander, P. Plasmon Modes of Nanosphere Trimers and Tetramers. *J. Phys. Chem. B* **2006**, *110*, 12302–12310.
- (12) Barrow, S. J.; Collins, S. M.; Rossouw, D.; Funston, A. M.; Botton, G. A.; Midgley, P. A.; Mulvaney, P. Electron Energy Loss Spectroscopy Investigation into Symmetry in Gold Trimer and Tetramer Plasmonic Nanoparticle Structures. *ACS Nano* **2016**, *10*, 8552–8563.
- (13) Ma, W.; Xu, L.; de Moura, A. F.; Wu, X.; Kuang, H.; Xu, C.; Kotov, N. A. Chiral Inorganic Nanostructures. *Chem. Rev.* **2017**, *117*, 8041–8093.
- (14) Coenen, T.; Arango, F. B.; Koenderink, A. F.; Polman, A. Directional Emission from a Single Plasmonic Scatterer. *Nat. Commun.* **2014**, *5*, 3250.
- (15) Atwater, H. A.; Polman, A. Plasmonics for Improved Photovoltaic Devices. *Nat. Mater.* **2010**, *9*, 205–213.
- (16) Krenn, J. R.; Dereux, A.; Weeber, J. C.; Bourillot, E.; Lacroute, Y.; Goudonnet, J. P.; Schider, G.; Gotschy, W.; Leitner, A.; Aussenegg, F. R.; et al. Squeezing the Optical Near-Field Zone by Plasmon Coupling of Metallic Nanoparticles. *Phys. Rev. Lett.* **1999**, *82*, 2590–2593.
- (17) Maier, S. A.; Kik, P. G.; Atwater, H. A.; Meltzer, S.; Harel, E.; Koel, B. E.; Requicha, A. A. G. Local Detection of Electromagnetic Energy Transport Below the Diffraction Limit in Metal Nanoparticle Plasmon Waveguides. *Nat. Mater.* **2003**, *2*, 229–232.
- (18) Gobin, A. M.; Lee, M. H.; Halas, N. J.; James, W. D.; Drezek, R. A.; West, J. L. Near-Infrared Resonant Nanoshells for Combined Optical Imaging and Photothermal Cancer Therapy. *Nano Lett.* **2007**, *7*, 1929–1934.
- (19) Nie, S.; Emory, S. R. Probing Single Molecules and Single Nanoparticles by Surface-Enhanced Raman Scattering. *Science* **1997**, *275*, 1102–1106.
- (20) Stiles, P. L.; Dieringer, J. A.; Shah, N. C.; Van Duyne, R. P. Surface-Enhanced Raman Spectroscopy. *Annu. Rev. Anal. Chem.* **2008**, *1*, 601–626.
- (21) Sherry, L. J.; Jin, R.; Mirkin, C. A.; Schatz, G. C.; Van Duyne, R. P. Localized Surface Plasmon Resonance Spectroscopy of Single Silver Triangular Nanoprisms. *Nano Lett.* **2006**, *6*, 2060–2065.
- (22) Féliidj, N.; Grand, J.; Laurent, G.; Aubard, J.; Lévi, G.; Hohenau, A.; Galler, N.; Aussenegg, F. R.; Krenn, J. R. Multipolar Surface Plasmon Peaks on Gold Nanotriangles. *J. Chem. Phys.* **2008**, *128*, 094702.
- (23) Rodríguez-Fernández, J.; Novo, C.; Myroshnychenko, V.; Funston, A. M.; Sánchez-Iglesias, A.; Pastoriza-Santos, I.; Pérez-Juste, J.; García de Abajo, F. J.; Liz-Marzán, L. M.; Mulvaney, P. Spectroscopy, Imaging and Modeling of Individual Gold Decahedra. *J. Phys. Chem. C* **2009**, *113*, 18623–18631.
- (24) Hartschuh, A. Tip-Enhanced Near-Field Optical Microscopy. *Angew. Chem., Int. Ed.* **2008**, *47*, 8178–8191.
- (25) Rang, M.; Jones, A. C.; Zhou, F.; Li, Z.-Y.; Wiley, B. J.; Xia, Y.; Raschke, M. B. Optical Near-Field Mapping of Plasmonic Nanoprisms. *Nano Lett.* **2008**, *8*, 3357–3363.
- (26) Viarbitskaya, S.; Teulle, A.; Marty, R.; Sharma, J.; Girard, C.; Arbouet, A.; Dujardin, E. Tailoring and Imaging the Plasmonic Local Density of States in Crystalline Nanoprisms. *Nat. Mater.* **2013**, *12*, 426–432.
- (27) Volpe, G.; Cherukulappurath, S.; Juanola Parramon, R.; Molina-Terriza, G.; Quidant, R. Controlling the Optical Near Field of Nanoantennas with Spatial Phase-Shaped Beams. *Nano Lett.* **2009**, *9*, 3608–3611.
- (28) Piazza, L.; Lummen, T. T. A.; Quiñonez, E.; Murooka, Y.; Reed, B. W.; Barwick, B.; Carbone, F. Simultaneous Observation of the Quantization and the Interference Pattern of a Plasmonic Near-Field. *Nat. Commun.* **2015**, *6*, 6407.
- (29) Barwick, B.; Flannigan, D. J.; Zewail, A. H. Photon-Induced Near-Field Electron Microscopy. *Nature* **2009**, *462*, 902.
- (30) García de Abajo, F. J. Optical Excitations in Electron Microscopy. *Rev. Mod. Phys.* **2010**, *82*, 209–275.
- (31) Kociak, M.; Stéphan, O. Mapping Plasmons at the Nanometer Scale in an Electron Microscope. *Chem. Soc. Rev.* **2014**, *43*, 3865–3883.
- (32) Losquin, A.; Lummen, T. T. A. Electron Microscopy Methods for Space-, Energy-, and Time-Resolved Plasmonics. *Front. Phys.* **2017**, *12*, 127301.
- (33) Nelayah, J.; Kociak, M.; Stéphan, O.; García de Abajo, F. J.; Tencé, M.; Henrard, L.; Taverna, D.; Pastoriza-Santos, I.; Liz-Marzán, L. M.; Colliex, C. Mapping Surface Plasmons on a Single Metallic Nanoparticle. *Nat. Phys.* **2007**, *3*, 348–353.
- (34) Gu, L.; Sigle, W.; Koch, C. T.; Ögüt, B.; van Aken, P. A.; Talebi, N.; Vogelgesang, R.; Mu, J.; Wen, X.; Mao, J. Resonant Wedge-Plasmon Modes in Single-Crystalline Gold Nanoplatelets. *Phys. Rev. B: Condens. Matter Mater. Phys.* **2011**, *83*, 195433.
- (35) Duan, H.; Fernández-Domínguez, A. I.; Bosman, M.; Maier, S. A.; Yang, J. K. W. Nanoplasmonics: Classical down to the Nanometer Scale. *Nano Lett.* **2012**, *12*, 1683–1689.
- (36) Losquin, A.; Zagonel, L. F.; Myroshnychenko, V.; Rodríguez-González, B.; Tencé, M.; Scarabelli, L.; Förstner, J.; Liz-Marzán, L. M.; García de Abajo, F. J.; Stéphan, O.; et al. Unveiling Nanometer Scale Extinction and Scattering Phenomena through Combined Electron Energy Loss Spectroscopy and Cathodoluminescence Measurements. *Nano Lett.* **2015**, *15*, 1229–1237.
- (37) Nicoletti, O.; de la Peña, F.; Leary, R. K.; Holland, D. J.; Ducati, C.; Midgley, P. A. Three-Dimensional Imaging of Localized Surface Plasmon Resonances of Metal Nanoparticles. *Nature* **2013**, *502*, 80–84.
- (38) Keast, V. J.; Walhout, C. J.; Pedersen, T.; Shahcheraghi, N.; Cortie, M. B.; Mitchell, D. R. G. Higher Order Plasmonic Modes Excited in Ag Triangular Nanoplates by an Electron Beam. *Plasmonics* **2016**, *11*, 1081–1086.
- (39) Yamamoto, N.; Araya, K.; Toda, A.; Sugiyama, H. Light Emission from Surfaces, Thin Films and Particles Induced by High-Energy Electron Beam. *Surf. Interface Anal.* **2001**, *31*, 79–86.
- (40) Denisyuk, A. I.; Adamo, G.; MacDonald, K. F.; Edgar, J.; Arnold, M. D.; Myroshnychenko, V.; Ford, M. J.; García de Abajo, F. J.; Zheludev, N. I. Transmitting Hertzian Optical Nanoantenna with Free-Electron Feed. *Nano Lett.* **2010**, *10*, 3250–3252.

- (41) Chaturvedi, P.; Hsu, K. H.; Kumar, A.; Fung, K. H.; Mabon, J. C.; Fang, N. X. Imaging of Plasmonic Modes of Silver Nanoparticles Using High-Resolution Cathodoluminescence Spectroscopy. *ACS Nano* **2009**, *3*, 2965–2974.
- (42) Das, P.; Chini, T. K.; Pond, J. Probing Higher Order Surface Plasmon Modes on Individual Truncated Tetrahedral Gold Nanoparticle Using Cathodoluminescence Imaging and Spectroscopy Combined with FDTD Simulations. *J. Phys. Chem. C* **2012**, *116*, 15610–15619.
- (43) Knight, M. W.; Liu, L.; Wang, Y.; Brown, L.; Mukherjee, S.; King, N. S.; Everitt, H. O.; Nordlander, P.; Halas, N. J. Aluminum Plasmonic Nanoantennas. *Nano Lett.* **2012**, *12*, 6000–6004.
- (44) Osorio, C. I.; Coenen, T.; Brenny, B. J. M.; Polman, A.; Koenderink, A. F. Angle-Resolved Cathodoluminescence Imaging Polarimetry. *ACS Photonics* **2016**, *3*, 147–154.
- (45) Kociak, M.; Zagonel, L. F. Cathodoluminescence in the Scanning Transmission Electron Microscope. *Ultramicroscopy* **2017**, *176*, 112–131.
- (46) Chu, M.-W.; Myroshnychenko, V.; Chen, C.-H.; Deng, J.-P.; Mou, C.-Y.; García de Abajo, F. J. Probing Bright and Dark Surface-Plasmon Modes in Individual and Coupled Noble Metal Nanoparticles Using an Electron Beam. *Nano Lett.* **2009**, *9*, 399–404.
- (47) Rossouw, D.; Couillard, M.; Vickery, J.; Kumacheva, E.; Botton, G. A. Multipolar Plasmonic Resonances in Silver Nanowire Antennas Imaged with a Subnanometer Electron Probe. *Nano Lett.* **2011**, *11*, 1499–1504.
- (48) Zagonel, L. F.; Mazzucco, S.; Tencé, M.; March, K.; Bernard, R.; Laslier, B.; Jacopin, G.; Tchernycheva, M.; Rigutti, L.; Julien, F. H.; et al. Nanometer Scale Spectral Imaging of Quantum Emitters in Nanowires and Its Correlation to Their Atomically Resolved Structure. *Nano Lett.* **2011**, *11*, 568–573.
- (49) Yamamoto, N. *The Transmission Electron Microscope*; InTech: London, United Kingdom, 2012; pp 251–274.
- (50) Guzzinati, G.; Béché, A.; Lourenço-Martins, H.; Martin, J.; Kociak, M.; Verbeeck, J. Probing the Symmetry of the Potential of Localized Surface Plasmon Resonances with Phase-Shaped Electron Beams. *Nat. Commun.* **2017**, *8*, 14999.
- (51) Talebi, N.; Sigle, W.; Vogelgesang, R.; Koch, C. T.; Fernández-López, C.; Liz-Marzán, L. M.; Ögüt, B.; Rohm, M.; van Aken, P. A. Breaking the Mode Degeneracy of Surface Plasmon Resonances in a Triangular System. *Langmuir* **2012**, *28*, 8867–8873.
- (52) Yamamoto, N. Development of High-Resolution Cathodoluminescence System for STEM and Application to Plasmonic Nanostructures. *Microscopy* **2016**, *65*, 282–295.
- (53) García de Abajo, F. J.; Howie, A. Retarded Field Calculation of Electron Energy Loss in Inhomogeneous Dielectrics. *Phys. Rev. B: Condens. Matter Mater. Phys.* **2002**, *65*, 115418.
- (54) Myroshnychenko, V.; Carbó-Argibay, E.; Pastoriza-Santos, I.; Pérez-Juste, J.; Liz-Marzán, L. M.; García de Abajo, F. J. Modelling the Optical Response of Highly Faceted Metal Nanoparticles with a Fully 3D Boundary Element Method. *Adv. Mater.* **2008**, *20*, 4288–4293.
- (55) Myroshnychenko, V.; Nelayah, J.; Adamo, G.; Geuquet, N.; Rodríguez-Fernández, J.; Pastoriza-Santos, I.; MacDonald, K. F.; Henrard, L.; Liz-Marzán, L. M.; Zheludev, N. I.; et al. Plasmon Spectroscopy and Imaging of Individual Gold Nanodecahedra: A Combined Optical Microscopy, Cathodoluminescence, and Electron Energy-Loss Spectroscopy Study. *Nano Lett.* **2012**, *12*, 4172–4180.
- (56) Yamamoto, N.; Araya, K.; García de Abajo, F. J. Photon Emission from Silver Particles Induced by a High-Energy Electron Beam. *Phys. Rev. B: Condens. Matter Mater. Phys.* **2001**, *64*, 205419.
- (57) Gómez-Medina, R.; Yamamoto, N.; Nakano, M.; García de Abajo, F. J. Mapping Plasmons in Nanoantennas via Cathodoluminescence. *New J. Phys.* **2008**, *10*, 105009.
- (58) Kumar, A.; Fung, K.-H.; Mabon, J. C.; Chow, E.; Fang, N. X. Excitation and Imaging of Resonant Optical Modes of Au Triangular Nanoantennas Using Cathodoluminescence Spectroscopy. *J. Vac. Sci. Technol., B: Nanotechnol. Microelectron.: Mater., Process., Meas., Phenom.* **2010**, *28*, C6C21–C6C25.
- (59) Schmidt, F. P.; Ditzbacher, H.; Hofer, F.; Krenn, J. R.; Hohenester, U. Morphing a Plasmonic Nanodisk into a Nanotriangle. *Nano Lett.* **2014**, *14*, 4810–4815.
- (60) Kawasaki, N.; Meuret, S.; Weil, R.; Lourenço-Martins, H.; Stéphan, O.; Kociak, M. Extinction and Scattering Properties of High-Order Surface Plasmon Modes in Silver Nanoparticles Probed by Combined Spatially Resolved Electron Energy Loss Spectroscopy and Cathodoluminescence. *ACS Photonics* **2016**, *3*, 1654–1661.
- (61) Levine, I. N. *Molecular Spectroscopy*; Wiley-Interscience: London, United Kingdom, 1975.
- (62) Awada, C.; Popescu, T.; Douillard, L.; Charra, F.; Perron, A.; Yockell-Lelièvre, H.; Baudrion, A.-L.; Adam, P.-M.; Bachelot, R. Selective Excitation of Plasmon Resonances of Single Au Triangles by Polarization-Dependent Light Excitation. *J. Phys. Chem. C* **2012**, *116*, 14591–14598.
- (63) Zhang, W.; Gallinet, B.; Martin, O. J. F. Symmetry and Selection Rules for Localized Surface Plasmon Resonances in Nanostructures. *Phys. Rev. B: Condens. Matter Mater. Phys.* **2010**, *81*, 233407.
- (64) García de Abajo, F. J.; Kociak, M. Probing the Photonic Local Density of States with Electron Energy Loss Spectroscopy. *Phys. Rev. Lett.* **2008**, *100*, 106804.
- (65) Kuttge, M.; Vesseur, E. J. R.; Koenderink, A. F.; Lezec, H. J.; Atwater, H. A.; García de Abajo, F. J.; Polman, A. Local Density of States, Spectrum, and Far-Field Interference of Surface Plasmon Polaritons Probed by Cathodoluminescence. *Phys. Rev. B: Condens. Matter Mater. Phys.* **2009**, *79*, 113405.
- (66) Losquin, A.; Kociak, M. Link between Cathodoluminescence and Electron Energy Loss Spectroscopy and the Radiative and Full Electromagnetic Local Density of States. *ACS Photonics* **2015**, *2*, 1619–1627.
- (67) Yamamoto, N.; Ohtani, S.; García de Abajo, F. J. Gap and Mie Plasmons in Individual Silver Nanospheres near a Silver Surface. *Nano Lett.* **2011**, *11*, 91–95.
- (68) Coenen, T.; Vesseur, E. J. R.; Polman, A. Angle-Resolved Cathodoluminescence Spectroscopy. *Appl. Phys. Lett.* **2011**, *99*, 143103.
- (69) Ferrell, R. Predicted Radiation of Plasma Oscillations in Metal Films. *Phys. Rev.* **1958**, *111*, 1214–1222.
- (70) Boardman, A. D. *Electromagnetic Surface Modes*; Wiley: New York, 1982.
- (71) Johnson, P. B.; Christy, R. W. Optical Constants of the Noble Metals. *Phys. Rev. B* **1972**, *6*, 4370–4379.